

PAPER

Experimental study of cross phase influence on Reynolds stress in the HL-2A tokamak


To cite this article: D. Guo *et al* 2018 *Nucl. Fusion* **58** 026015

View the [article online](#) for updates and enhancements.

You may also like

- [Spatio-temporal structure of turbulent Reynolds stress zonal flow drive in 3D magnetic configuration](#)
B Schmid, P Manz, M Ramisch et al.
- [Reduction of edge plasma turbulence via cross-phase decrease by zonal fields](#)
Chang-Bae Kim, Chan-Yong An and Byunghoon Min
- [Potential Vorticity Mixing in a Tangled Magnetic Field](#)
Chang-Chun Chen and Patrick H. Diamond

Experimental study of cross phase influence on Reynolds stress in the HL-2A tokamak

D. Guo¹, L. Nie¹, R. Ke^{1,2}, M. Xu^{1,a}, Z.H. Wang¹, T. Long¹, Y.F. Wu^{1,3}, B.D. Yuan^{1,3}, S.B. Gong^{1,3}, H. Liu^{1,3} and HL-2A Team¹

¹ Southwestern Institute of Physics, PO Box 432, Chengdu 610041, People's Republic of China

² Department of Engineering Physics, Tsinghua University, Beijing, China, 10084, People's Republic of China

³ Department of Nuclear Science and Technology, University of Science and Technology of China, Jinzhai Road 96#, 230026, Hefei, People's Republic of China

E-mail: minxu@swip.ac.cn

Received 23 May 2017, revised 16 September 2017

Accepted for publication 24 October 2017

Published 21 December 2017



Abstract

The cross phase between radial velocity perturbation \tilde{v}_r and poloidal velocity perturbation \tilde{v}_θ plays an important role in the radial distribution of Reynolds stress. Recently, a novel theory of cross-phase dynamics predicts that, depending on the strength of the $\mathbf{E} \times \mathbf{B}$ shearing, the cross phase can stay in two different states: phase locked state (weak shear regime) and phase slipping state (strong shear regime). For the first time we divided Reynolds stress into three parts, turbulence fluctuation, cross phase and coherence between \tilde{v}_r and \tilde{v}_θ , and studied their relative influences on Reynolds stress in different regimes. The profile of Reynolds stress and its three parts are measured separately by using multi-tipped Langmuir probe array. We observe that the three parts contribute to the radial distribution of Reynolds stress differently. In strong shear layer, the cross phase is randomly scattered across the layer—a signature of incoherent phase slips. Correspondingly, the radial distribution of the Reynolds stress is determined by the cross phase dynamics. In the weak shear region, the cross phase tends to stay in a coherent state (i.e. the phase locked state), where the turbulence fluctuation and coherence play a more important role. Besides, a direct relation between the coherence and the cross phase scattering is observed. Once the scattering of the cross phase increases, the coherence decreases.

Keywords: Reynolds stress, cross phase, coherence, turbulence fluctuation, HL-2A, phase scattering

(Some figures may appear in colour only in the online journal)

1. Introduction

One of the major challenges for the research towards a fusion power plant is the understanding and control of plasma turbulence that leads to anomalous transport of particles and energy. Vigorous experimental and theoretical efforts worldwide have led to a compelling model of $\mathbf{E} \times \mathbf{B}$ shear suppressing turbulence and reducing transport [1–7]. Increasingly, the effect of

sheared poloidal flows at the plasma boundary has been identified as a crucial element in edge turbulence dynamics. The shear flow driven by the radial electric field suppresses turbulence transport in two ways: one is to decrease the amplitude of turbulent fluctuations [8, 9], which has been studied widely; the other way is to change the phase relation between temperature or density fluctuation and its radial velocity fluctuation [10–12]. While the physical mechanism of the interaction between shear flow and turbulence cross phase is still under study. The turbulent flux of momentum—or Reynolds stress—is a mechanism

^a Author to whom any correspondence should be addressed.

responsible for the generation of sheared flow by turbulence [13–19]. Diamond and Kim proposed a theory to explain the flow generation in turbulent plasmas by small-scale turbulence fluctuations via the Reynolds stress [13]. Poloidal flow could be accelerated if the turbulent Reynolds stress is nonzero and has a radial gradient. Thus, measurement of the Reynolds stress especially its profile is helpful to predict shear flow in plasmas. Since shear flow is the key element for the suppression of turbulence and improvement of plasma confinement, study of Reynolds stress is significant for understanding the improved confinement scenarios such as H-mode confinement regimes.

As Reynolds stress is proportional to fluctuation intensity, it is easy to understand the dependence of Reynolds stress on the variation of fluctuation intensity, i.e. $|\tilde{v}_r|$ and $|\tilde{v}_\theta|$. Reynolds stress should also depend on the cross phase and coherence between \tilde{v}_r and \tilde{v}_θ [10]. Terry *et al* studied the general properties of cross-phase suppression in the strong shear regime by using the generic non-mode-specific model of Biglari, Diamond, and Terry (BDT) [12]. This research suggests that the cross phase in the transport flux is strongly reduced in the strong shear regime (shearing rate $>$ eddy turnover rate), leading to significant transport suppression. Experiments on TEXTOR tokamak measured the turbulent temperature fluctuation and reveal that turbulent heat flux depends on the fluctuation intensity, coherence and cross phase [10]. By using bias electrode they studied the shear influence on heat flux and its components, but they analyzed the coherence and the cross phase as a unity. So far, there is no detailed experimental report on the coherence, cross phase and their relations with shear intensity. Recently, Z.B. Guo and P.H. Diamond proposed a ‘phase locking & phase slip’ model [20] to explain the mechanism for the transition from ELMy H mode to Quiescent (Q) H mode. They studied the transition by calculating the cross phase dynamics of the Peeling-ballooning (PB) driven heat flux in the presence of an $\mathbf{E} \times \mathbf{B}$ shear flow. This methodology is in distinct contrast to the conventionally employed eigenmode and quasilinear analysis, which implicitly take the cross phase as fixed. And they predict the underlying relation between $\mathbf{E} \times \mathbf{B}$ shearing rate, coherence and cross phase dynamics.

In this paper, Reynolds stress is divided into three parts (turbulence fluctuation, cross phase and coherence) and their relative influences to Reynolds stress in different regimes are studied experimentally in detail. And for the first time we observed the ‘phase locking & phase slip’ phenomenon in a tokamak plasma. In this work, both radial and poloidal velocity perturbations and radial electric field are measured on HL-2A tokamak near the last closed flux surface (LCFS) by using multi-tipped Langmuir probes. The profiles of turbulence fluctuation, cross phase and the coherence between \tilde{v}_r and \tilde{v}_θ are presented and their contributions to Reynolds stress in both strong shear and weak shear regions are discussed.

This paper is organized as follows. In section 2, it will present the mathematical definition of turbulence fluctuation, cross phase and coherence. In addition, diagnostic tools used for this work is also presented. In section 3, it will present the experimental results and comparisons of turbulence fluctuation, cross phase and coherence contributions to Reynolds stress profile in both strong shear layer and weak shear region. A summary of this work is given in section 4.

2. Experimental setup

By Fourier transforming \tilde{v}_r and \tilde{v}_θ , we get

$$\tilde{v}_r(t) = \text{Re} \left(\sum_{\omega} v_r(\omega) \cdot e^{i\omega t} \right) \quad (1a)$$

$$\tilde{v}_\theta(t) = \text{Re} \left(\sum_{\omega} v_\theta(\omega) \cdot e^{i\omega t} \right) \quad (1b)$$

Ensemble-averaged Reynolds stress could be written as

$$\langle \tilde{v}_r \tilde{v}_\theta \rangle = \left\langle \text{Re} \sum_{\omega} P_{\tilde{v}_r \tilde{v}_\theta}(\omega) \right\rangle \quad (2)$$

where ‘ $\langle \rangle$ ’ denotes the ensemble average, $P_{\tilde{v}_r \tilde{v}_\theta}(\omega)$ means the cross power of \tilde{v}_r and \tilde{v}_θ which could be divided into three parts: turbulence fluctuation, cosine of cross phase average and coherence.

$$\tilde{v}_r \tilde{v}_\theta = \sigma_{\tilde{v}_r} \sigma_{\tilde{v}_\theta} \cdot \cos \langle \varphi \rangle \cdot \langle \gamma \rangle. \quad (3)$$

In this equation, $\sigma_{\tilde{v}_r}$ and $\sigma_{\tilde{v}_\theta}$ are standard deviation of \tilde{v}_r and \tilde{v}_θ in each window. What we need to pay attention to is that $\langle \varphi \rangle$ and $\langle \gamma \rangle$ are the averaged cross phase and coherence between \tilde{v}_r and \tilde{v}_θ in frequency domain. Their ensemble-averaged value could be computed by equations (4) and (5) where *angle* means the arctangent of the imaginary and real part of the sum of $P_{\tilde{v}_r \tilde{v}_\theta}(\omega)$.

$$\langle \varphi \rangle = \text{angle} \left(\sum_{\omega} (P_{\tilde{v}_r \tilde{v}_\theta}(\omega)) \right) \quad (4)$$

$$\langle \gamma \rangle = \frac{\sum_{\omega} |P_{\tilde{v}_r \tilde{v}_\theta}|}{\sum_{\omega} \sigma_{\tilde{v}_r} \cdot \sum_{\omega} \sigma_{\tilde{v}_\theta}}. \quad (5)$$

HL-2A is a divertor tokamak and its major and minor radii are $R = 1.65$ m, $a = 0.4$ m, and the line averaged density can be operated at $6 \times 10^{19} \text{ m}^{-3}$. Heating power are 3 MW of neutral beam injection, 2 MW of LHCD, and 5 MW of electron cyclotron resonance heating. Fueling systems are multiple pellet injection and supersonic molecular beams injections [21–24]. In the experiment, the plasma current is opposite to the direction of the toroidal magnetic field. Figure 1(a) is the cross section of the HL-2A tokamak. A fast reciprocating probe system is installed on the outer middle plane of the HL-2A and it can move inwards and outwards at a speed of 1 m s^{-1} . This system could measure as long as 5 centimeters inside the LCFS as shown by the red box in figure 1(a). With this system, we could get the spatial distribution of the edge plasma parameters along the radial direction during a discharge with sampling rate of 1 MS s^{-1} . The measurements were conducted by using a multi-tipped probe array composed of 3×4 probe tips [6, 9] (3 tips in the poloidal direction and 4 tips in the radial direction) facing the plasma current I_p . With a proper setup, this probe array can simultaneously measure plasma density n_e , potential V_p , temperature T_e [25, 26], Reynolds stress Rs , and particle flux Γ . The distance between two adjacent probe tips is 5 mm in the poloidal direction and 2.5 mm in the radial direction, which makes the 3×4 probe array smaller than a

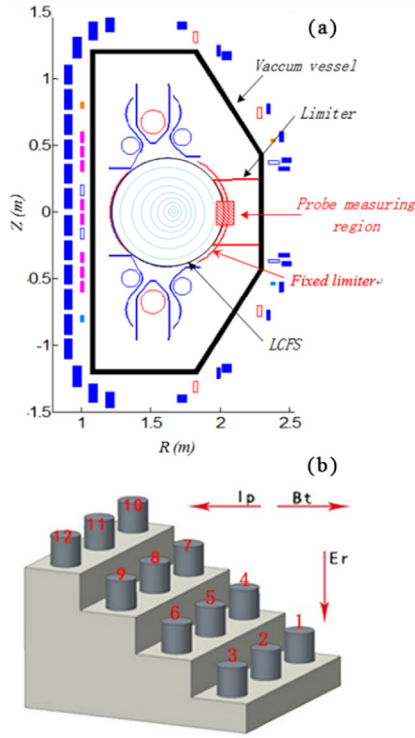


Figure 1. (a) cross section of HL-2A tokamak (b) four-stage langmuir probe array.

typical turbulent eddy in both poloidal and radial directions (the typical turbulence correlation length is larger than 3 cm in the poloidal direction and $\sim 1.0\text{--}1.5\text{ cm}$ in the radial direction in HL-2A tokamak edge plasma). The deepest stage (#4) is a set of triple probe to measure $T_e = (V_{10}^- - V_{f,11})/\ln 2$ and $n_e = I_{10,12}/(0.61 \cdot e \cdot A_{\text{eff}} \cdot \sqrt{kT_e/m_i})$ where $I_{10,12} = (V_{10}^- - V_{12}^+)/R_s$ is the ion saturation current and $A_{\text{eff}} = 8\text{ mm}^2$ is the effective collecting area of each tip; m_i is the mass of ion; $R_s = 50\ \Omega$ is the sample resistance. Radial and poloidal velocity fluctuation is estimated by $\tilde{v}_r = (\tilde{v}_{f,7} - \tilde{v}_{f,9})/2d_\theta B_t$, and $\tilde{v}_\theta = (\tilde{v}_{f,5} - \tilde{v}_{f,11})/2d_r B_t$ where ‘ \sim ’ represents the fluctuation with its frequency ranges from 20 kHz to 80 kHz (hereafter neglected, unless otherwise noted). $B_t \approx 1.35\text{ T}$ is the amplitude of the toroidal magnetic field. In this study, plasma potential can be expressed as $\tilde{v}_p = \tilde{v}_f + \alpha \tilde{T}_e$ in which $\alpha = 2.5$. We estimated the influence of temperature fluctuation on the measurement of plasma potential and find that in L mode discharge on HL-2A, the \tilde{v}_f fluctuation level is about 4 times that of $\alpha \tilde{T}_e$. We assume that the influence of electron temperature fluctuation has little contribution to the measurement of plasma potential [29].

3. Experimental results

3.1. Equilibrium profiles

This experiment is operated in L-mode discharge with a plasma current $I_p \sim 150\text{ kA}$, a toroidal magnetic field $B_t \sim 1.35\text{ T}$, a line averaged density $n_e \sim 0.3 \times 10^{19}\text{ m}^{-3}$ and these parameters remain constant during the process of the probe moving into plasma as marked by the yellow box in figure 2. This shooting

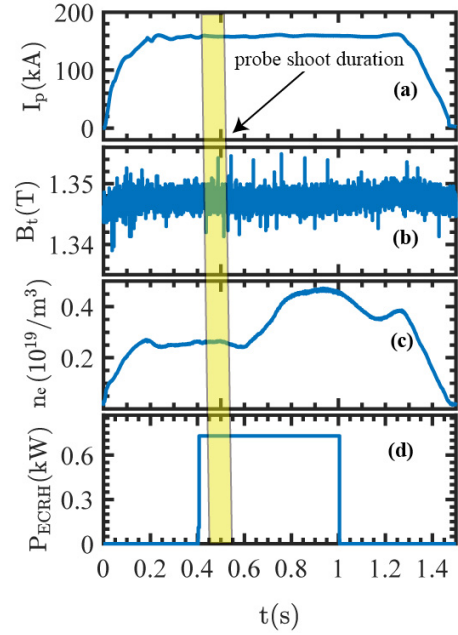


Figure 2. Time evolution of different parameters on HL-2A under L-mode discharge with limiter configuration (a) plasma current I_p (b) toroidal magnetic field B_t (c) line average plasma density n_e (d) ECRH heating power. Langmuir probe shoots into plasma at 0.45 s and stops at 0.53 s with constant speed of 1 m s^{-1} as marked by the yellow box.

process has a constant velocity of 1 m s^{-1} which can be used to infer the depth that probe shoots into LCFS. In this process 700 kW ECRH heating power is applied to the plasma.

In this shot, the position of LCFS is determined by the point where poloidal velocity changes its direction from the ion diamagnetic drift to electron diamagnetic drift. Figure 3 shows the equilibrium profiles of the electron density n_e , electron temperature T_e and poloidal velocity v_θ . The profile of v_θ is obtained from the equation $\frac{\nabla \phi_p \times B_t}{B^2}$ and we checked this by TDE (time delay estimation) method [27, 28]. As is shown in figure 3(c), there is little difference in the measurement of v_θ by two different methods. v_θ increases quickly from $r - r_{\text{LCFS}} = 0.6\text{ cm}$ to $r - r_{\text{LCFS}} = -1.2\text{ cm}$ and changes its direction at the position of LCFS. The radial electric field shear (or flow shear) peaks in this region. Figure 4 shows the $\tilde{v}_{f,11}$ fluctuation power spectrum and our turbulence analysis is based on the frequency ranging from 20 to 80 kHz.

3.2. Experimental measurements of Reynolds stress and its components (turbulence fluctuation, cross phase, coherence)

From equation (3) we know that Reynolds stress could be divided into three parts, thus it means that the profile of Reynolds stress is determined by three factors: the turbulence fluctuation $\sigma_{\tilde{v}_r} \sigma_{\tilde{v}_\theta}$, the cosine of cross phase average $\cos \langle \varphi \rangle$, and the coherence $\langle \gamma \rangle$ between \tilde{v}_r and \tilde{v}_θ . In order to compare their influences on Reynolds stress separately, experimental measurements of these three physical parameters are plotted in figure 5. The blue curve and red curve in figure 5(a) are spatial evolution of Reynolds stress $\langle \tilde{v}_r \tilde{v}_\theta \rangle$ and $\sigma_{\tilde{v}_r} \sigma_{\tilde{v}_\theta} \cdot \cos \langle \varphi \rangle \cdot \langle \gamma \rangle$ respectively. They are equal in the whole profile which means

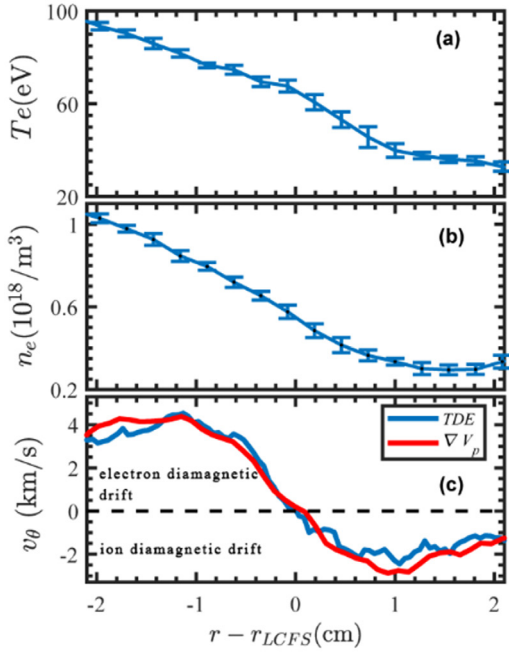


Figure 3. Profiles of (a) electron temperature T_e , (b) density n_e and (c) poloidal velocity estimated by TDE method (blue) and $\frac{\nabla \phi_p \times B_t}{B^2}$ (red).

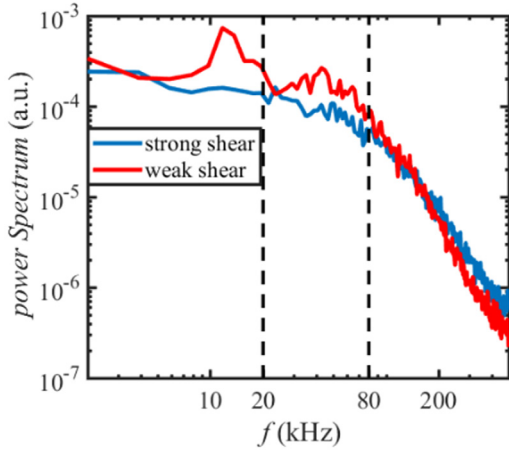


Figure 4. Floating potential power spectrum in strong shear layer (blue) and weak shear region (red).

that it is reasonable to divide Reynolds stress into the three parts. Turbulence fluctuation increases quickly first then saturates and changes slowly, while the profile of Reynolds stress does not change much from 2 cm outside LCFS to 0.5 cm inside LCFS. From $r - r_{LCFS} = -0.5$ cm to $r - r_{LCFS} = -2$ cm, Reynolds stress changes its sign from negative to positive and increases quickly. Turbulence fluctuation first decreases and then increases in this region. This reveals that turbulence fluctuation is not the only reason to determine the radial distribution of Reynolds stress. Comparison between the profile of Reynolds stress and $\cos \langle \varphi \rangle$ shows good consistency in the shear layer from 0.6 cm outside LCFS to 1.2 cm inside LCFS as marked by the brown shadow. The two curves increase and decrease at the same time and they change their signs at the same position. While $\sigma_{\tilde{v}_r} \sigma_{\tilde{v}_\theta}$ and $\langle \gamma \rangle$ are fixed to a certain value

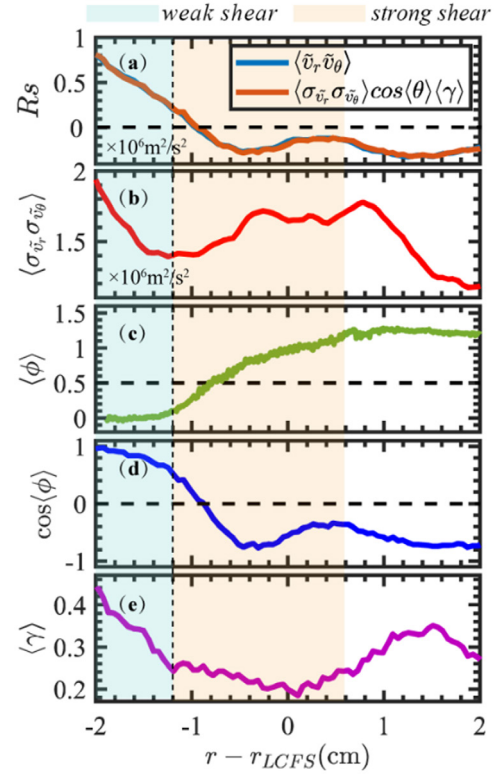


Figure 5. Spatial evolution of (a) Reynolds stress computed by $\langle \tilde{v}_r \tilde{v}_\theta \rangle$ and $\langle \sigma_{\tilde{v}_r} \sigma_{\tilde{v}_\theta} \rangle \cdot \cos \langle \varphi \rangle \cdot \langle \gamma \rangle$; (b) turbulence fluctuation $\langle \sigma_{\tilde{v}_r} \sigma_{\tilde{v}_\theta} \rangle$. Here we use the standard deviation of each window to stand for the turbulent fluctuation amplitude. ‘ $\langle \rangle$ ’ means the window average results over 1024 points. (c) Cross phase average. (d) Cosine of cross phase average (e) coherence between \tilde{v}_r and \tilde{v}_θ .

and change not much in the shear layer. In the weak shear region from $r - r_{LCFS} = -1.2$ cm to $r - r_{LCFS} = -2$ cm marked by blue shadow, this relation changes. $\langle \varphi \rangle$ gets to be zero and $\cos \langle \varphi \rangle$ saturates to 1. On the contrary, $\langle \sigma_{\tilde{v}_r} \sigma_{\tilde{v}_\theta} \rangle$ and $\langle \gamma \rangle$ increases quickly in this region. This suggests that turbulence fluctuation, cross phase and coherence impact the radial distribution of Reynolds stress differently in different regimes.

3.3. The influence of $\mathbf{E} \times \mathbf{B}$ shear on the cross phase scattering in both strong and weak shear region

‘Phase locking & phase slip’ model predicts that, depending on the strength of the $\mathbf{E} \times \mathbf{B}$ shear, the cross phase can stay in two different states. The impact of $\mathbf{E} \times \mathbf{B}$ shear on the cross phase scattering and the coherence between \tilde{v}_r and \tilde{v}_θ is shown in figure 6. Figure 6(c) is the cross power profile between \tilde{v}_r and \tilde{v}_θ and its distribution on phase difference. In the shear layer -1.2 cm $< r - r_{LCFS} < 0.6$ cm, the cross phase average changes quickly from $\sim \pi$ to ~ 0 , and the cross phase scattering is larger than in other regions. The value of coherence between \tilde{v}_r and \tilde{v}_θ is small and changes not much in this region. In the weak shear region where \mathbf{E}_r shear is small, the cross phase is much more concentrated than in the shear layer. At the same time the coherence peaks in this region which means that the cross phase between \tilde{v}_r and \tilde{v}_θ is more fixed with a quite low scattering level. This experimental observation consists with the theory prediction. In weak shear regime,

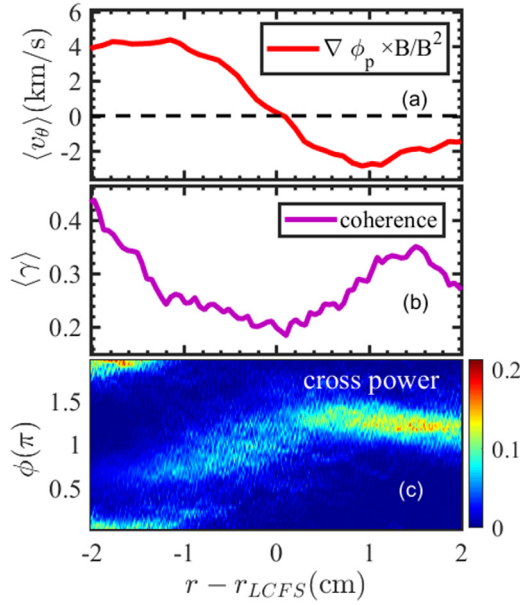


Figure 6. Equilibrium profile of (a) poloidal velocity v_θ . (b) Coherence average $\langle \gamma \rangle$ and (c) phase evolution of Cross phase between \tilde{v}_r and \tilde{v}_θ .

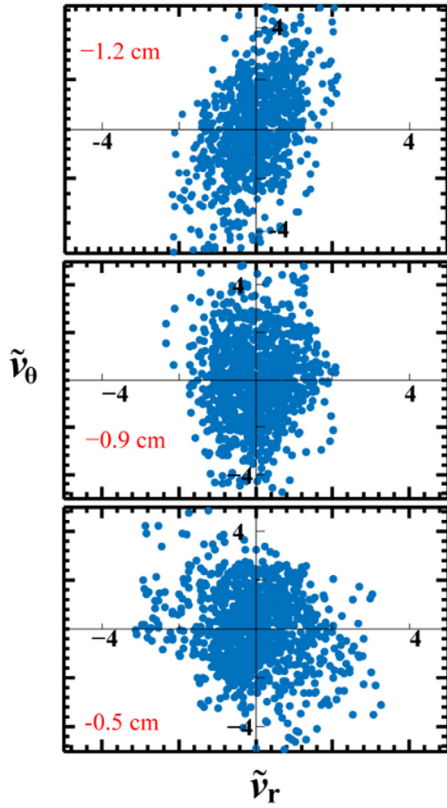


Figure 7. Scatter plots of \tilde{v}_r and \tilde{v}_θ at 3 different positions (a) $r - r_{LCFS} = -1.2$ cm (b) $r - r_{LCFS} = -0.9$ cm (c) $r - r_{LCFS} = -0.5$ cm. Each position contains 1 ms data (1000 points) as sample.

as turbulence fluctuation is large and cross phase between \tilde{v}_r and \tilde{v}_θ is fixed with little variation, the profile of Reynolds stress is dominantly determined by the turbulence fluctuation. This corresponds to the ‘phase locking’ state. In strong shear regime, the cross phase scattering is in direct proportion to the

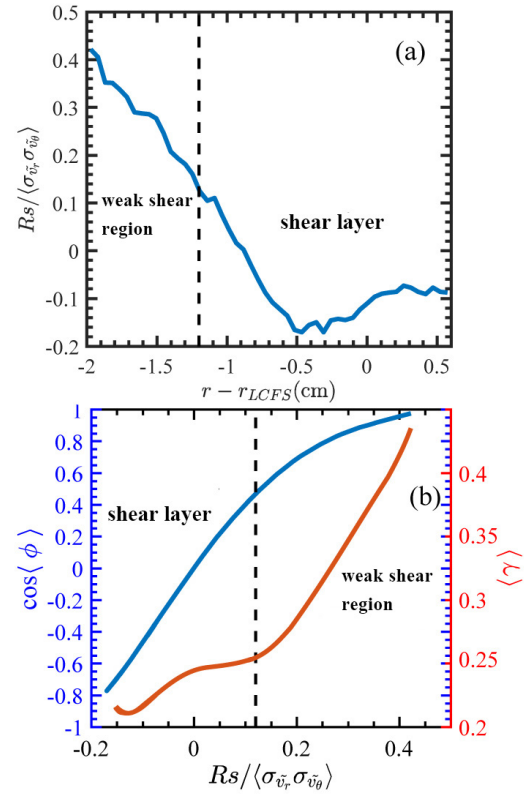


Figure 8. (a) radial distribution of normalized $Rs / \langle \sigma_{\tilde{v}_r} \sigma_{\tilde{v}_\theta} \rangle$, the left side of the dashed line is the weak shear region and the right side is the shear layer. We observe that $Rs / \langle \sigma_{\tilde{v}_r} \sigma_{\tilde{v}_\theta} \rangle$ is greater than ~ 0.14 in weak shear region and smaller than ~ 0.14 in shear layer. (b) Relation between $\cos \langle \phi \rangle$ and $Rs / \langle \sigma_{\tilde{v}_r} \sigma_{\tilde{v}_\theta} \rangle$. In the shear layer, $\cos \langle \phi \rangle$ plays a dominant role in determining the variation of normalized Reynolds stress. And in the weak shear region, $\langle \gamma \rangle$ becomes more important.

shear strength. And the cross phase scattering would in turn impact the coherence between \tilde{v}_r and \tilde{v}_θ . Once the scattering of cross phase increases, the coherence decreases. Therefore, the coherence could work as an index of the scattering level of cross phase. Once the coherence increases, the scattering level of cross phase decreases. As turbulence fluctuation is relatively small in strong shear regime, the radial distribution of Reynolds stress is mainly determined by the cross phase. This is corresponding to the ‘phase slip’ state.

3.4. Phase modulation on the radial distribution of Reynolds stress in shear layer

The change of turbulent Reynolds stress can also be seen in figure 7 that shows the joint probability density functions (PDFs) of radial and poloidal velocity fluctuations. As Reynolds stress increases from negative to positive in the shear layer, the tilting angle of the joint PDF also changes. Each scatter plot in figure 7 contains 1 ms period of data with 1 MHz sample rate. At position $r - r_{LCFS} = -1.2$ cm the scatter points mainly fall into the first and third quadrants which means \tilde{v}_r and \tilde{v}_θ have the same sign and accordingly $RS > 0$. It is just the opposite in figure 7(c) at position $r - r_{LCFS} = -0.5$ cm, the scatter points mostly fall into the second and fourth quadrants

and $R_s < 0$; at position $r - r_{LCFS} = -0.9$ cm, the scatter points fall into the four quadrants in average which indicates that the cross phase average is $\pi/2$ or $3\pi/2$ thereby and $R_s = 0$.

In order to give a clear comparison between the three components' contributions to Reynolds stress, radial distribution of normalized $R_s / \langle \sigma_{\tilde{v}_r} \sigma_{\tilde{v}_\theta} \rangle$ is presented in figure 8(a). As $\langle \sigma_{\tilde{v}_r} \sigma_{\tilde{v}_\theta} \rangle$ is positive in both shear layer and weak shear region, Reynolds stress is positive in weak shear region and negative in shear layer (-1.2 cm $< r - r_{LCFS} < -0.5$ cm is the transitional region between the two regions), $R_s / \langle \sigma_{\tilde{v}_r} \sigma_{\tilde{v}_\theta} \rangle$ is positive in the weak shear region (greater than 0.14) and negative in shear layer (smaller than 0.14). The deeper inside the weak shear region, the turbulence fluctuation can contribute more to the value of Reynolds stress. It is different in shear layer that when -0.5 cm $< r - r_{LCFS} < 0.6$ cm, the coefficient between Reynolds stress and turbulence fluctuation is stable. This coefficient is about -0.1 . In the transitional region where the coefficient changes from negative to positive, the influence of turbulence fluctuation on Reynolds stress becomes less important because the coefficient is around zero. Blue curve in figure 8(b) shows the relation between $\cos \varphi$ and $R_s / \langle \sigma_{\tilde{v}_r} \sigma_{\tilde{v}_\theta} \rangle$. This curve linear growth in shear layer and saturates in the weak shear region. While $\langle \gamma \rangle$, the red curve in figure 8(b), shows the opposite influence on $R_s / \langle \sigma_{\tilde{v}_r} \sigma_{\tilde{v}_\theta} \rangle$. It does not change much in the shear layer while increases quickly in the weak shear region. According to the analysis above, we have a clear comparison between the impacts of the turbulence fluctuation, cross phase and the coherence between \tilde{v}_r and \tilde{v}_θ on the radial distribution of Reynolds stress. The cross phase plays a dominant role in determining the variation of Reynolds stress in the shear layer while the turbulence fluctuation and coherence become more important to determine the radial distribution of Reynolds stress in the weak shear region.

4. Summary

The edge turbulent Reynolds stress and shear flows have been investigated on HL-2A tokamak L-mode discharge by using a multi-tipped Langmuir probe array. Reynolds stress is divided into three parts and their contributions to Reynolds stress were experimentally evaluated. Radial distribution of Reynolds stress is consistent with the product of turbulence fluctuation, cosine of cross phase average and coherence between \tilde{v}_r and \tilde{v}_θ . Experimental observation shows that the turbulence fluctuation, cross phase and coherence between \tilde{v}_r and \tilde{v}_θ have different contributions to the radial distribution of Reynolds stress. In strong shear layer, the cross phase is randomly scattered across the layer—a signature of incoherent phase slips. Correspondingly, the radial distribution of the Reynolds stress is determined by the cross phase dynamics. In the weak shear region, the cross phase tends to stay in a coherent state, where the turbulence fluctuation and coherence play a more important role. This is for the first time we observe 'phase locking & phase slip' theory in experiment. Besides, a direct relation between the coherence and the cross phase scattering is observed, once the scattering of the cross phase increases, the coherence decreases.

Acknowledgments

We are grateful to Z.B. Guo and P.H. Diamond for useful discussions. This work is supported by the National Natural Science Foundation of China under Grant Nos. 11375053, 11705052, 11575055 and 11611130164; The National Key Research and Development Program of China under Grant No 2017YFE0300405; the International S&T Cooperation program of China under grant No. 2015DFA61760; and the Chinese National Fusion Project for ITER under grant No.2013GB111005 and 2013GB107001.

ORCID iDs

D. Guo  <https://orcid.org/0000-0001-6562-8841>

References

- [1] Wagner F. 2007 A quarter-century of H-mode studies *Plasma Phys. Control. Fusion* **49** B1–33
- [2] Tynan G.R., Fujisawa A. and Mckee G. 2009 A review of experimental drift turbulence studies *Plasma Phys. Control. Fusion* **51** 113001
- [3] Terry P. 2000 Suppression of turbulence and transport by sheared flow *Rev. Mod. Phys.* **72** 109
- [4] Burrell K.H. 1997 Effects of $E \times B$ velocity shear and magnetic shear on turbulence and transport in magnetic confinement devices *Phys. Plasmas* **4** 1499–518
- [5] Kim J.Y. *et al* 1996 Poloidal shear flow effect on toroidal ion temperature gradient mode: a theory and simulation *Phys. Plasmas* **3** 3689
- [6] Yan Z. *et al* 2010 Shear flow and drift wave turbulence dynamics in a cylindrical plasma device *Phys. Plasmas* **17** 032302
- [7] Hahn T. *et al* 1999 Shearing rate of time-dependent $E \times B$ flow *Phys. Plasmas* **6** 922–6
- [8] Xu G.S. *et al* 2011 First evidence of the role of zonal flows for the L–H transition at marginal input power in the EAST Tokamak *Phys. Rev. Lett.* **107** 125001
- [9] Xu M. *et al* 2011 Generation of a sheared plasma rotation by emission, propagation, and absorption of drift wave packets *Phys. Rev. Lett.* **107** 055003
- [10] Boedo J.A. *et al* 2000 Suppression of temperature fluctuations and energy barrier generation by velocity shear *Phys. Rev. Lett.* **84** 2630–3
- [11] Moyer R.A. *et al* 1995 Beyond paradigm: turbulence, transport, and the origin of the radial electric field in low to high confinement mode transitions in the DIII-D tokamak *Phys. Plasmas* **2** 2397
- [12] Terry P., Newman D. and Ware A. 2001 Suppression of transport cross phase by strongly sheared flow *Phys. Rev. Lett.* **87** 185001
- [13] Diamond P.H. and Kim Y.B. 1991 Theory of mean poloidal flow generation by turbulence *Phys. Fluids B* **3** 1626
- [14] Shukla P.K., Yu M.Y. and Spatschek K.H. 1981 Interaction of magnetostatic and electrostatic convective cells *Phys. Rev. A* **23** 3247–50
- [15] Shats M.G. *et al* 2000 Inward turbulent transport produced by positively sheared radial electric field in stellarators *Phys. Rev. Lett.* **84** 6042–5
- [16] Wilcox R.S. *et al* 2016 Intrinsic plasma rotation and Reynolds stress at the plasma edge in the HSX stellarator *Nucl. Fusion* **56** 036002

- [17] Yan Z. *et al* 2010 Intrinsic rotation from a residual stress at the boundary of a cylindrical laboratory plasma *Phys. Rev. Lett.* **104** 065002
- [18] Holland C. *et al* 2002 Evidence for Reynolds-stress driven shear flows using bispectral analysis: theory and experiment *Plasma Phys. Control. Fusion* **44** A453
- [19] Holland C., Tynan G., Fonck R., McKee G.R., Candy J. and Waltz R.E. 2007 Zonal-flow-driven nonlinear energy transfer in experiment and simulation *Phys. Plasmas* **14** 056112
- [20] Guo Z.B. and Diamond P.H. 2015 From phase locking to phase slips: a mechanism for a quiescent H mode *Phys. Rev. Lett.* **114** 145002
- [21] Yang Q.W. *et al* 2007 Overview of HL-2A experiment results *Nucl. Fusion* **47** S635–44
- [22] Ding X.T. *et al* 2006 New diagnostic systems on HL-2A *Rev. Sci. Instrum.* **77** 10F528
- [23] Yan L. *et al* 2006 Novel design for zonal flow probe arrays in the HL-2A Tokamak *Rev. Sci. Instrum.* **77** 113501
- [24] Yan L. *et al* 2005 Fast reciprocating probe system on the HL-2A Tokamak *Rev. Sci. Instrum.* **76** 093506
- [25] Hutchinson I.H. 2002 *Principles of Plasma Diagnostics* 2 edn (Cambridge: University of Cambridge)
- [26] Balbin R., Hidalgo C., Pedrosa M., García-Cortés I. and Vega J. 1992 Measurement of density and temperature fluctuations using a fast-swept Langmuir probe *Rev. Sci. Instrum.* **63** 4605–7
- [27] Holland C. *et al* 2004 Investigation of the time-delay estimation method for turbulent velocity inference *Rev. Sci. Instrum.* **75** 4278–80
- [28] Yu J. *et al* 2007 Examination of the velocity time-delay-estimation technique *J. Nucl. Mater.* **363** 728–32
- [29] Jun C., Long-Wen Y., Wen-Yu H., Jun Q. and Kai-Jun Z. 2007 Edge particle flux with temperature fluctuation in the HL-2A tokamak *Chinese Phys. Lett.* **24** 3191